




Insights on forming N,O-coordinated Cu single-atom catalysts for electrochemical reduction CO₂ to methane

Yanming Cai^{1,3}, Jiaju Fu^{1,3}, Yang Zhou^{2,3}, Yu-Chung Chang², Qianhao Min ^{1✉}, Jun-Jie Zhu ¹, Yuehe Lin ^{2✉} & Wenlei Zhu^{2✉}

Single-atom catalysts (SACs) are promising candidates to catalyze electrochemical CO₂ reduction (ECR) due to maximized atomic utilization. However, products are usually limited to CO instead of hydrocarbons or oxygenates due to unfavorable high energy barrier for further electron transfer on synthesized single atom catalytic sites. Here we report a novel partial-carbonization strategy to modify the electronic structures of center atoms on SACs for lowering the overall endothermic energy of key intermediates. A carbon-dots-based SAC margined with unique CuN₂O₂ sites was synthesized for the first time. The introduction of oxygen ligands brings remarkably high Faradaic efficiency (78%) and selectivity (99% of ECR products) for electrochemical converting CO₂ to CH₄ with current density of 40 mA·cm⁻² in aqueous electrolytes, surpassing most reported SACs which stop at two-electron reduction. Theoretical calculations further revealed that the high selectivity and activity on CuN₂O₂ active sites are due to the proper elevated CH₄ and H₂ energy barrier and fine-tuned electronic structure of Cu active sites.

¹State Key Laboratory of Analytical Chemistry for Life Science, School of Chemistry and Chemical Engineering, Nanjing University, Nanjing 210023, People's Republic of China. ²School of Mechanical and Materials Engineering, Washington State University, Pullman, WA 99164, USA. ³These authors contributed equally: Y. Cai, J. Fu, Y. Zhou. ✉email: minqianhao@nju.edu.cn; yuehe.lin@wsu.edu; wenlei.zhu@wsu.edu

Electrochemical CO₂ reduction (ECR) is becoming a viable way of both storing electric energy and removing extra CO₂ in the atmosphere. However, unsatisfied product selectivity on cathode remains one of the major stumbling blocks present for commercialization^{1,2}. Owing to the uniform coordination structures and unique electronic properties of metal centers, single-atom catalysts (SACs) have demonstrated excellent selectivity in various catalytic reactions^{3–7}. As promising candidates, SACs have been extensively explored as ECR catalysts, which boosts the product selectivity up to nearly 100%^{8,9}. Though great progresses have been achieved, previous studies are generally limited to two-electron reduction products such as CO and HCOOH because of the lack of accurate manipulation in single-atom structures. For instance, traditional atomic metal–nitrogen-carbon moieties (M–N–Cs) are supported in micron-sized carbon-based substrates and form through the redispersion of aggregated metal nanoparticles under high temperature (above 800 °C)^{10,11}. This process is so extreme that it causes the N- and C-containing precursors to lose the original structures and rebuild with metal atoms into the most thermodynamically preferred form, the commonly reported MN_xC₄ moiety^{12,13}. In consequence, high-temperature pyrolysis makes diverse precursors to fail to tune the coordination environments which determine the intrinsic properties of obtained SACs¹⁴. Recently, Guan et al. reported a temperature-tuned N-coordination strategy to manipulate single-atom Cu–N_x coordination¹⁵. Two neighboring Cu–N₂ sites were synthesized to form C₂H₄ through a C–C bond formation on two Cu atoms. But much improvement is needed in their product selectivity and Faradaic efficiency due to the ambiguous catalytic sites and the adverse Cu electronic properties when coordinated with N^{16,17}. Although extensive efforts have been devoted, to our knowledge, fine tuning of SAC coordination environments to accurately change catalytic selectivity with multiple electron-reducing products remains a great challenge and are rarely investigated till now.

Conventional molecular catalysts as well-defined metal complexes possess acutely tailorable structures^{18,19}, which prevail over SACs. However, they are typically involved in homogeneous catalysis^{20–22}, which limits the catalytic performance by outer sphere electron transfer from the electrode in electrochemical catalysis^{23,24}. To tackle this problem, researchers tried to immobilize metal phthalocyanines on carbon nanotubes to create heterogeneous catalytic surfaces^{24–26}. Nevertheless, this strategy is limited to hydrophobic complexes that can resist dissolving in aqueous electrolytes. Therefore, it is of great significance to develop a more general approach to immobilize all kinds of molecular catalysts on electrodes.

Herein, we present a carbon dots (CDs)-supported SAC prepared by a low-temperature calcining process from metal–organic complexes, which transforms the carbon containing molecular complexes into solid-state CDs while preserving the coordination environments of metal atoms. We chose copper disodium EDTA, i.e., Na₂[Cu(EDTA)] as a demonstration (Fig. 1a). By the process of such a semi-transformed strategy, the single-atom Cu-embedded carbon dots (Cu-CDs) with coordination of two N and two O were obtained, which was the first-time introduction of N,O ligands. As a result, the catalyst exhibited the extraordinary selectivity for electrochemical reduction of CO₂ to CH₄ over a wide potential range from –1.14 to –1.64 V vs. RHE (reversible hydrogen electrode), as more than 99% of the CO₂ reduction products were CH₄. Besides, Cu-CDs presented high CH₄ Faradaic efficiency (78%) and turn over frequency (2370 h^{–1}) at –1.44 and –1.64 V, respectively. Density functional theory (DFT) calculations unveiled that the separation of CH₄ limiting potential from other products enables exclusive producing of CH₄. To our knowledge, this is the first report on the fabrication of SACs on functionalized CDs.

Results

Synthesis and structural characterization. The Cu-CDs were synthesized by calcinating Na₂[Cu(EDTA)]·2H₂O at 250 °C for 2 h (details in Methods), which was the minimum carbonation temperature to form CDs (Supplementary Fig. 1)²⁷. The obtained Cu-CDs had a thickness between 0.7 and 1.8 nm, corresponding to 1–3 atomic layers²⁸ (Supplementary Fig. 2), and transmission electron microscopes (TEM) images showed a lateral size distribution of 2–5 nm and a lattice spacing of 0.21 nm corresponding to (100) interplanar spacing^{29,30} of graphite (Fig. 1b, c and Supplementary Fig. 3). The atomic absorption spectra verified that the Cu content in Cu-CDs prepared at 250 °C was 0.44 wt%. However, when the calcination temperature increased to 300 and 350 °C, the Cu contents were decreased to 0.35 and 0.22 wt%, which indicated the destruction of –COOH functional groups so that less Cu was chelated on CDs. Meanwhile, pristine CDs without Cu-doping were also synthesized from Na₂[H₂(EDTA)] precursor using the identical treatment, which exhibited a similar morphology as the Cu-CDs (Supplementary Fig. 4).

The dispersive Cu atoms on Cu-CDs was confirmed by aberration-corrected high-angle annular dark-field scanning transmission electron microscopy (HAADF-STEM) (Fig. 1d, e and Supplementary Figs. 5 and 6). As shown in Fig. 1e, atom-scale bright spots represent the location of single Cu atoms that are mainly distributed around the edge of the Cu-CD framework, supporting our functional groups anchored scheme. It is extremely difficult to capture HAADF-STEM image of CDs due to the fragile intrinsic and carbon contamination under the convergent electron beam. These are the highest definition pictures we can get under boosted scanning speed but we fail to carry out electron energy loss mapping. Furthermore, the powder X-ray diffraction (XRD) spectrum (Supplementary Fig. 7) also shows no apparent peak corresponding to metallic Cu or other copper-derived crystallines on the as-synthesized Cu-CDs. Thus, the CD-supported Cu SACs were successfully synthesized. To the best of our knowledge, it was the first time that single atoms had been observed in CDs.

Surface properties and electronic states of catalysts. To further investigate the atomic distribution and coordination environments of Cu atoms on Cu-CDs, spectral analyses were carried out. As shown in Fig. 2a, bands at ~3434, 1597, and 1120 cm^{–1} in infrared (IR) spectrum of Cu-CDs are associated with the ν_{O–H}, ν_{C=O}, and ν_{C–O} vibrations of COOH species, and the peak at around 1390 cm^{–1} denotes the typical C=N or C–N stretching vibrations^{31,32}. Compared with Na₂[Cu(EDTA)], Cu-CDs could be verified having the functional groups coordinated with Cu ions as Na₂[Cu(EDTA)], while the decrease in methylene antisymmetric stretching vibration at 2929 cm^{–1} indicated that the –CH₂– species were condensed into CDs after calcination. The same results were also deduced from X-ray photoelectron spectra (XPS) (Supplementary Fig. 8). With deconvolution of the C1s and N1s peaks, the quantitative results were given in Supplementary Table 1, indicating that the surfaces of Cu-CDs were modified by abundant C–O, C=O, and N–C species. The same functional groups were detected in pristine CDs (Supplementary Figs. 9 and 10). Although Cu-CDs and CDs were similar in N content, the Cu-CDs tended to have more pyridinic N than CDs because of the oxidation by Cu²⁺ ions (Supplementary Table 2 and Supplementary Fig. 11), and pyridinic N is considered as the anchoring site for CO₂ capture^{28,33,34}.

For Cu valence state, the high-resolution Cu 2p XPS spectra of both Cu-CDs and Na₂[Cu(EDTA)] showed the peaks at 932.5 eV (2p_{3/2}) and 952.5 eV (2p_{1/2}), respectively, which are associated

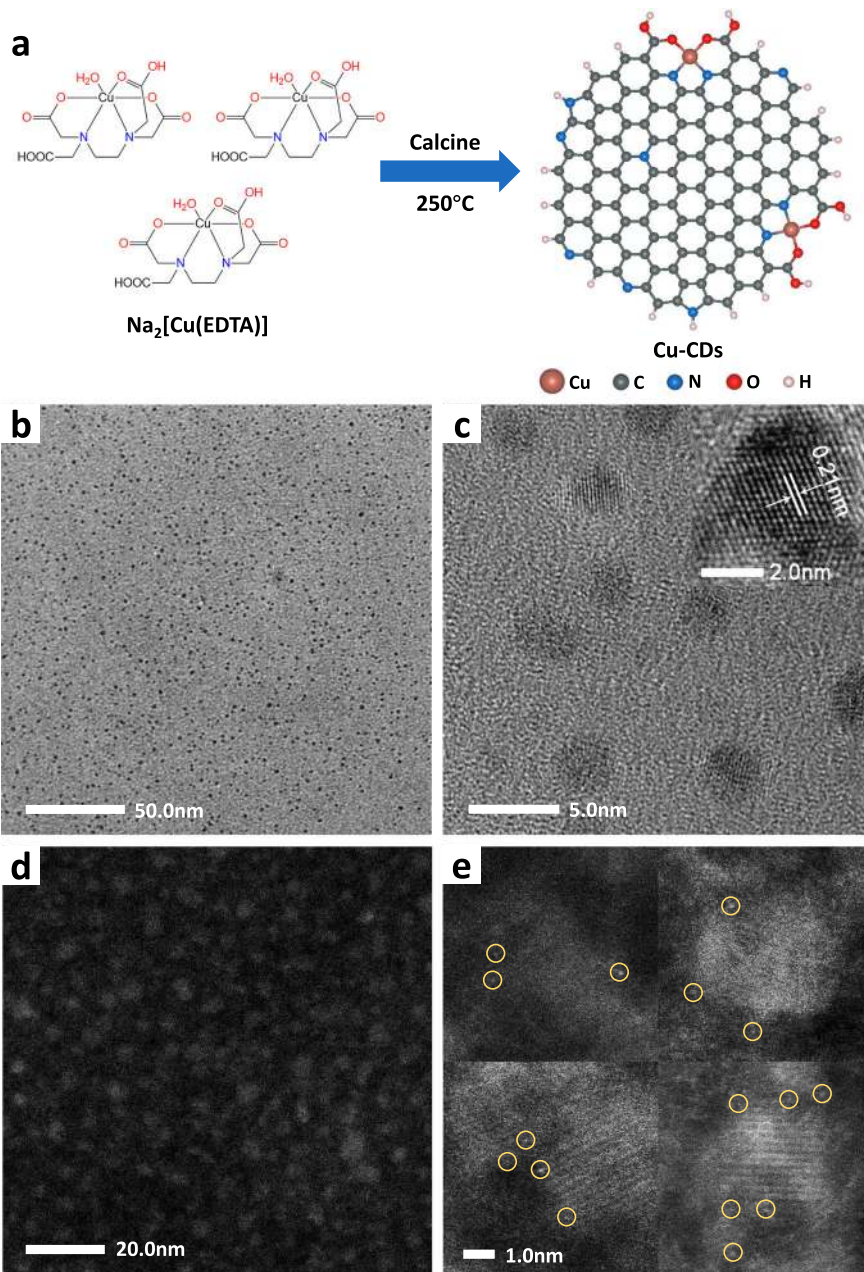


Fig. 1 Morphology characterization of the Cu-CD catalyst. **a** Scheme of the low-temperature calcining procedure for Cu-CD catalysts. **b** Large-field of view and **c** magnified view of TEM images (the inset is the crystal lattice). **d** Relatively large-field of view and **e** typical view of HAADF-STEM images of distributed single Cu atoms in carbon dots. Yellow circles in (**e**) indicates typical single Cu atoms.

with the Cu^+/Cu^0 state (Fig. 2b) rather than the Cu^{2+} state before coordinated by EDTA^{4-} . It is attributed to the strong covalent interactions between the Cu^{2+} -ligand bonds²⁷, causing the transfer of electrons from ligands to Cu^{2+} orbitals and the decrease in Cu $2p$ binding energy³⁵. The fine detail of Cu-CDs at the atomic level was further investigated by synchrotron X-ray absorption spectroscopy (XAS). As shown in Fig. 2c, the absorption edge position of Cu-CDs is located between that of Cu(II) phthalocyanine (CuPc) and Cu_2O , with a minor shift to the low-energy direction compared to $\text{Na}_2[\text{Cu}(\text{EDTA})]$. In agreement with the XPS results, the valence of Cu species in Cu-CDs is between +1 and +2, and also slightly lower than that of $\text{Na}_2[\text{Cu}(\text{EDTA})]$. For the extended X-ray absorption fine structure (EXAFS) spectra (Fig. 2d), the Cu-CD catalyst exhibited similar spectrum features to that of reference sample $\text{Na}_2[\text{Cu}(\text{EDTA})]$.

They both displayed one prominent peak at 1.5 Å that corresponds to the Cu–O/N first coordination shell. The peak at around 2.3 Å is attributed to the Cu–C scattering path in higher shells³⁶, and no Cu–Cu coordination peak at 2.2 Å could be detected. All of these suggested that the Cu center of Cu-CDs possesses comparable coordination environments to $\text{Na}_2[\text{Cu}(\text{EDTA})]$ whose center metal is coordinated by both N and O^{37,38}. The quantitative coordination configuration of Cu-CDs was further investigated by EXAFS curve fitting (Supplementary Fig. 12 and Supplementary Table 3). By comparing the fitting coordination number (CN) between $\text{Na}_2[\text{Cu}(\text{EDTA})]$ (CN = 4.3) and Cu-CDs (CN = 3.6), we could determine some detachment of coordination groups in Cu-CDs. But further unveiling the respective coordination number of N and O could be a trouble because of the similar bond length of

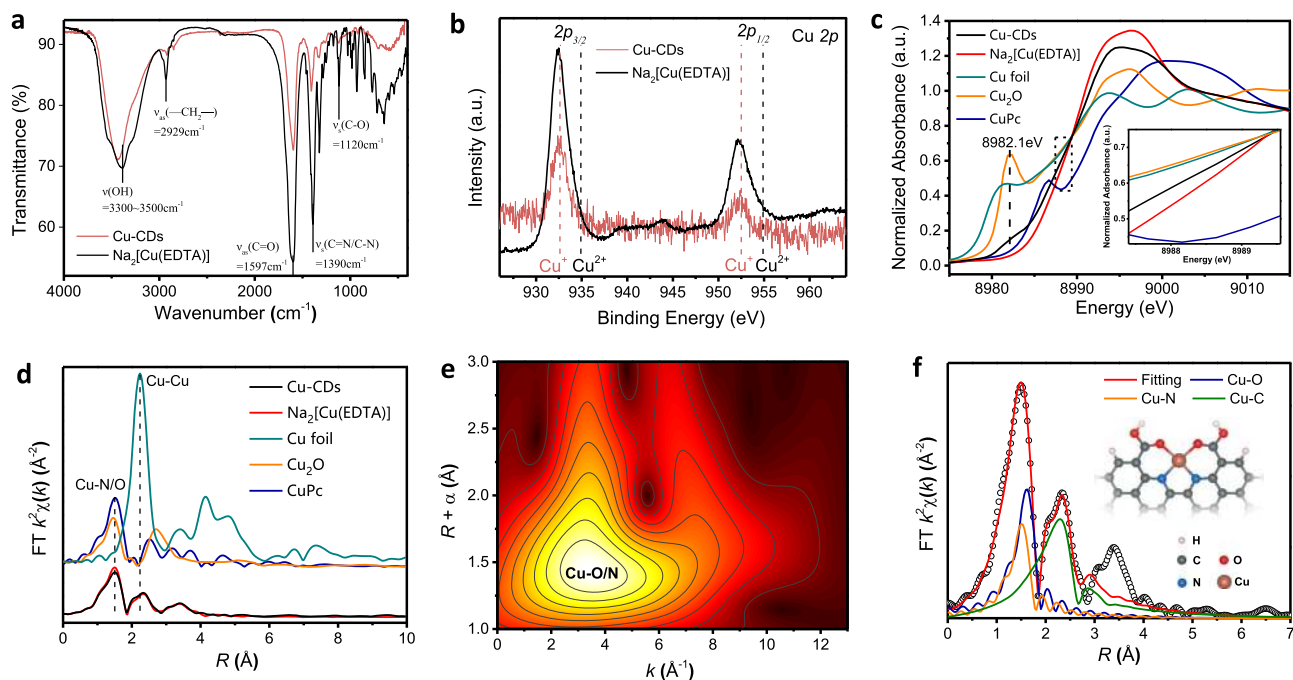


Fig. 2 Surface properties and electronic states studies. **a** FT-IR spectra and **b** high-resolution Cu 2p spectra of Cu-CDs and its precursor $\text{Na}_2[\text{Cu}(\text{EDTA})]$. **c** X-ray absorption near-edge structure (XANES) spectra and **d** Fourier transform (FT) EXAFS spectra at the Cu K-edge of Cu-CDs, $\text{Na}_2[\text{Cu}(\text{EDTA})]$, Cu foil, Cu_2O , and CuPc sample (inset is the magnified image of dashed box). **e** Wavelet transform (WT) of Cu-CDs. **f** EXAFS fitting curves of Cu-CDs in R space using backscattering paths of Cu-N, Cu-O, and Cu-C. The inset in (f) shows the structure of Cu sites in Cu-CDs.

Cu-N and Cu-O, even the wavelet transform (WT) of EXAFS (Fig. 2e) failed to discriminate the N and O signals in k -space. Thus, three backscattering paths of N, O, and C were employed to give the best-fitting analyses (Fig. 2f and Supplementary Table 4). It confirmed that the Cu center is coordinated with two N atoms and two O atoms (Supplementary Fig. 13 and Supplementary Table 5). Therefore, the Cu atomic structure model of Cu-CDs could be deduced and shown in the inset of Fig. 2f.

ECR performance. The electrocatalytic activity of the above-mentioned catalysts toward ECR were performed in an H cell employing CO_2 -saturated 0.5 M KHCO_3 aqueous solution as electrolyte (details in Supplementary Information). As described by the cyclic voltammetry (CV) curves in Fig. 3a, there was a significant cathodic current increase recorded in Cu-CD electrode after purged with CO_2 contrary to N_2 -saturated KHCO_3 solution. More importantly, different from the weak and broad waves between -0.5 V and -1.2 V observed in $\text{Na}_2[\text{Cu}(\text{EDTA})]$, there were no obvious Cu redox peaks in CV curves of Cu-CD and CuPc electrodes^{26,39}. Taken together, these results demonstrated that the Cu-CDs have a substantial catalytic effect on ECR. And it is worthwhile to note the similarity of the Cu active sites on Cu-CDs with the Cu^{2+} chelated in CuPc for avoiding rapid reduction like $\text{Na}_2[\text{Cu}(\text{EDTA})]$ at reducing potentials, which results from the heterogeneity of Cu-CDs and CuPc in aqueous electrolyte.

The gaseous and liquid products of ECR on Cu-CD catalysts were analyzed by gas chromatography (GC) and ^1H nuclear magnetic resonance (^1H NMR) spectroscopy, respectively, and converted into Faradaic efficiencies (FEs) in Fig. 3b. It is worth noting that at all selected potentials, formic acid was the only detected liquid product with FE less than 1% (Supplementary Fig. 14). Therefore, we did not mark the FEs of formic acid in the diagram. In fact, trace amounts of CO and C_2H_4 as by-products can also be ignored. During a broadly applied potential, the Cu-

CD electrode showed an unprecedented CO_2 reduction selectivity to CH_4 , as more than 99% of the CO_2 reduction products were CH_4 . Meanwhile, the FE(CH_4) of Cu-CDs increased as a more negative potential was applied, from $42 \pm 2\%$ at -1.14 V to a maximum of $78 \pm 2\%$ at -1.44 V with total current density of ~ 40 mA/cm^2 , and subsequently, it declined to $55 \pm 1\%$ at -1.66 V (Fig. 3b). Similar single-atom Cu sites prepared by adding CuCl_2 solution into pristine CDs ($\text{CDs} + \text{Cu}^{2+}$, details in Methods) had the same CH_4 selectivity as Cu-CDs whose by-products were prominently suppressed, except, a comparatively lower maximum FE(CH_4) of $53.4 \pm 0.8\%$ at -1.44 V (Fig. 3c). It indicates that the $\text{CDs} + \text{Cu}^{2+}$ shares the same active sites as Cu-CDs, and verified the coordinate interaction between copper ions and chelating ligands of CDs. We also confirmed carbon atoms in CH_4 was from CO_2 by using ^{13}C isotopic-labeling method (Supplementary Fig. 28). In contrast, CuPc showed significantly lower FEs and poorer CH_4 selectivity (Fig. 3d). The maximum FE(CH_4) was only around 15% at -1.14 V with total current density of ~ 10 mA/cm^2 , and only 75% of the CO_2 reduction products were CH_4 . As shown in Fig. 3e, the partial CH_4 current density of Cu-CDs is 25 times higher than that of CuPc at an applied potential of -1.64 V where Cu-CDs reach the maximum turnover frequency (TOF) of 2370 h^{-1} . These results indicated that the functional groups binding the Cu sites possess an ultra-stable +1 valence state, which prevents Cu species showing multi-valence so as to boost the selectivity of CH_4 ⁴⁰.

The calculation of stability of Cu-CDs was performed by continuous CO_2 reduction at the highest FE(CH_4) potential (-1.44 V, Fig. 3f). It is shown that after 6 h continuous test, the Cu-CDs could still remain 96% of the initial FE for CH_4 formation, while the FE(CH_4) of CuPc had apparent declines to only 4% after test. Afterward, the catalyst species on the Cu-CD electrode were washed with methanol and examined by HAADF-STEM. The image in Supplementary Fig. 15 clearly shows that the Cu atoms remained atomically dispersed. Moreover, UV-visible and fluorescence spectroscopy (Supplementary Fig. 16a, b) were

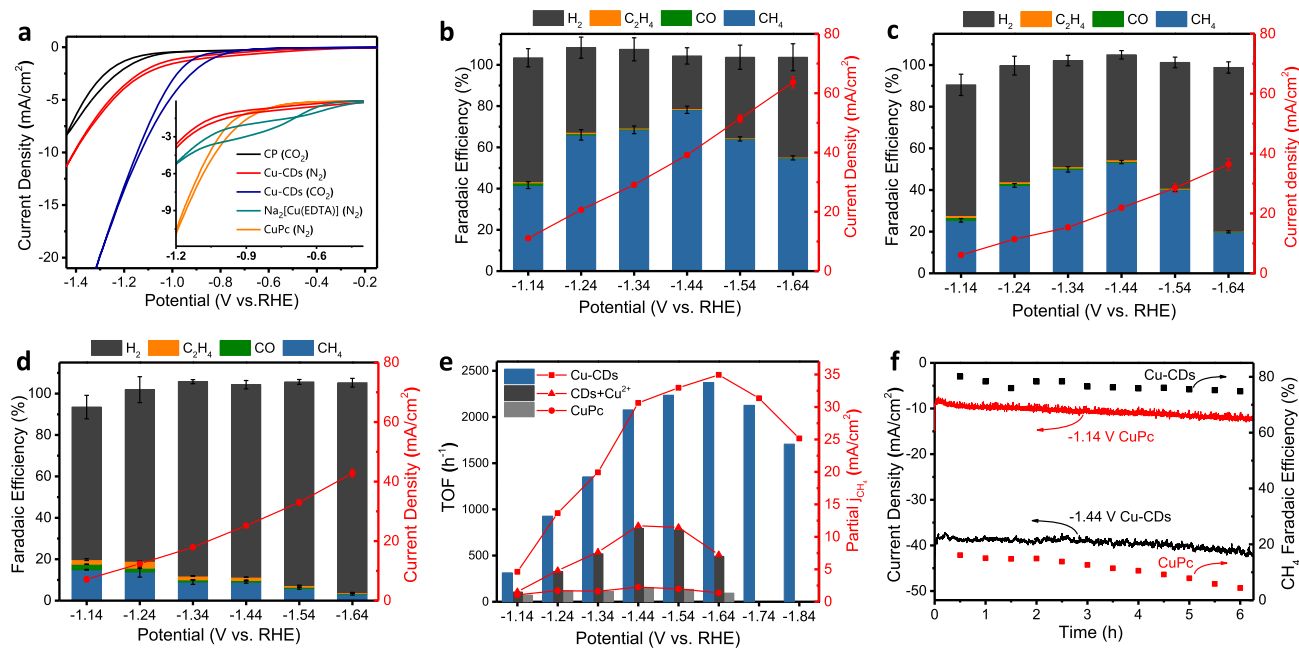


Fig. 3 CO₂ reduction in aqueous solution. **a** CV curves of bare carbon paper (CP), Cu-CDs, Na₂[Cu(EDTA)], and CuPc recorded in N₂- and CO₂-saturated 0.5 M KHCO₃ electrolyte with 10 mV/s scan speed. **b, c, d** Dependence of FE (left y-axis) and current density (based on geometric surface area, right y-axis) of **(b)** Cu-CDs, **(c)** CDs+Cu²⁺, and **(d)** CuPc on the applied potential. **e** Partial CH₄ current density plots and TOFs of Cu-CDs, CDs+Cu²⁺, and CuPc at different applied potentials. **f** Stability test of Cu-CDs and CuPc at their highest ECR Faradaic efficiency potentials.

also applied to investigate the Cu-CDs after ECR process. Because of the photophysical properties that the CDs give intense fluorescent emission while Cu coordination quenches the fluorescence, the spectrum shows no fluorescence recovery of the Cu-CDs after electrocatalysis, illustrating the survival of single-atom Cu. The pattern of UV-visible spectrum also remains unchanged, which is in good accord with the fluorescence results. XPS study of post-electrolyzed Cu-CDs verified that the Cu⁺ state is stable in functional groups' chelation after electrocatalysis (Supplementary Fig. 17).

Origin of electrocatalytic activity. A set of control experiments were carried out to exclude the contribution from other species such as in situ formed Cu nanoparticles. Firstly, pristine CDs were tested for CO₂ reduction under identical experimental conditions (Supplementary Fig. 18a, b). It was evident that the hydrogen dominated the products for the CD electrode at an applied potential of -1.14 to -1.64 V, which confirmed that the CDs only served as inert substrates to stabilize Cu ions. Besides, the result of CDs+Cu²⁺ (Fig. 3c) showed the same CH₄ selectivity as Cu-CDs, suggesting the role of Cu ions.

Then, ex situ XRD and scanning electron microscopy (SEM) characterizations were carried out to reflect any structural change. As expected, there was no diffraction peak of Cu₂O and Cu showed in the operated Cu-CD electrode (Supplementary Fig. 19c). SEM images showed a thin coat of Cu-CDs well dispersed on the surface of carbon fibers, and no existence of Cu₂O or Cu was found after the stability test (Supplementary Fig. 19b). To exclude any neglected metallic particles formed between carbon paper fibers, we used a bare carbon paper as a cathode and directly added Cu-CDs into the electrolyte then quickly switched it while electrolyzed. A time course of FEs polarized at -1.44 V was recorded in Supplementary Fig. 20. Due to Cu-CDs diffusion to the electrode, it turned out to have ~30% FE(CH₄) for Cu-CDs dispersed in the electrolyte. Then we switched the electrode to fresh 0.5 M KHCO₃ before 30 min, which showed a significant drop in FE. This experiment unambiguously confirmed that Cu or Cu₂O was not

deposited onto the cathode, and Cu-CDs were the catalyst that converts CO₂ to CH₄.

However, recent reports discovered that single-site Cu material could transiently convert into metallic Cu clusters that are considered as the active species for the catalysis under the working conditions. Intriguingly, this process is reversible upon release of the reduction potential^{26,41}, which makes ex situ observation fail to detect Cu nanoparticles. To verify whether such reconstruction also occurred in our material, in situ UV-visible spectroscopy was applied under the ECR condition (details in Methods). Firstly, CuPc was deposited on a transparent platinum sputtered quartz plate whose potential was dropped in steps from open circuit potential, OCP = 0.86 V vs. RHE to -1.14 V vs. RHE. At each potential, a series of UV-light spectra were continuously collected until they did not exhibit any variation, so as to reflect electrochemical stable states. According to Fig. 4a, there was a palpable change of spectra pattern with lower potentials applied. Comparison of the operando spectra with those of reference CuPc and phthalocyanine (Pc) confirmed the decomposition of CuPc under ECR condition. Furthermore, it was worth noting that the spectra experienced two main changes: reducing CuPc absorption at -0.64 V and rising B-bands absorption of Pc at -0.94 V, corresponding to the formation of Cu(I) and Cu(0), respectively, which was reported by in situ XAS observations²⁶. Accordingly, SEM characterizations were performed after the working electrode potential returned to 0.86 V (Supplementary Fig. 21). Like the previous study, well-dispersed nanoparticles emerged from cycled CuPc, which indicated that the same conversion took place during our operation. So we carried out in situ UV-visible measurements of Cu-CDs under the same conditions (Fig. 4b). Contrary to CuPc, decreasing electrode potential did not cause the shift of Cu-CD spectra to that of CDs without copper ion, and ex situ SEM did not observe any morphological changes (Supplementary Fig. 22). These experiments confirmed that it is single-site Cu that has intrinsic ECR activity in Cu-CDs rather than in situ formed Cu clusters.

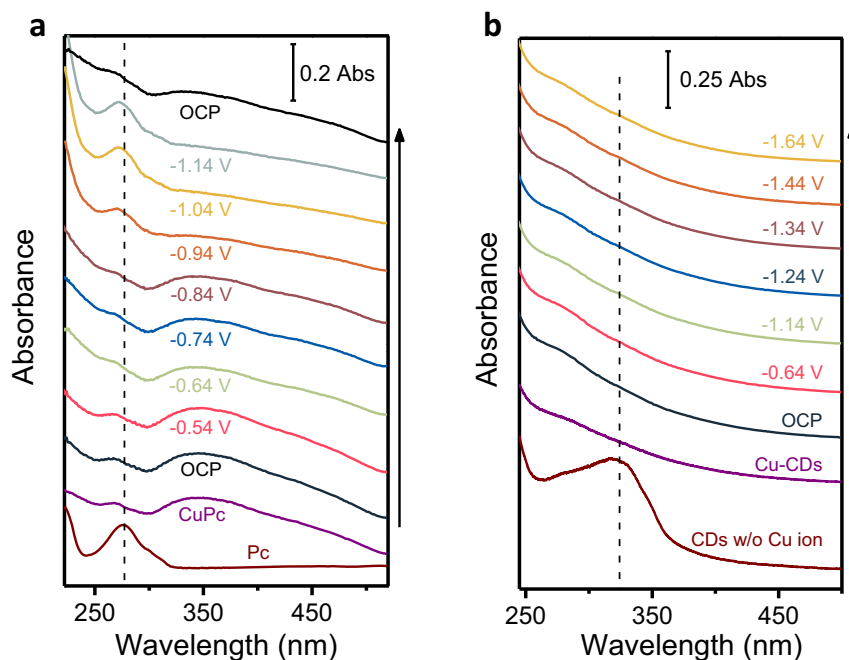


Fig. 4 In situ UV-visible measurements under electrocatalytic reaction conditions. **a** In situ UV-visible spectra of CuPc. **b** In situ UV-visible spectra of Cu-CDs. The spectra were collected with transmission mode by depositing samples on the transparent electrode.

DFT calculations. To further investigate the principles of structure–activity relationships laid in the CuN_2O_2 moieties of Cu-CDs, DFT calculations were performed. Firstly, we calculated the free energy of the lowest-energy pathways for electrochemical CO_2 -to- CH_4 reduction on CuN_2O_2 in comparison with that of conventional CuN_4 (Supplementary Fig. 23), and Cu(111) surface as a reference because the operando formed Cu clusters in CuPc. As shown in Fig. 5a, the introduction of CuN_2O_2 sites lowers the overall endothermic energy of intermediates for $^*\text{COOH}$ (1.56 eV) and $^*\text{COH}$ (2.58 eV) compared with that for CuN_4 (1.94 eV and 3.10 eV, respectively). However, compared with the pathway on Cu(111) surface, the energy barriers are still higher for effectively processing the formation of CH_4 , which cannot explain the selectivity and activity advantages of Cu-CDs over CuPc.

However, further calculating the free energy profiles of H_2 evolution reaction (HER) provided us a possible answer (Fig. 5b). The CuN_2O_2 sites show much higher formation energy for $^*\text{H}$ adsorption (1.46 eV) than that of CuN_4 (1.17 eV) and Cu(111) (0.20 eV) surface, which indicates that HER is well inhibited by CuN_2O_2 moieties even under high negative bias. In addition, the free energy profiles for possible by-products were also investigated (Supplementary Fig. 24). Their limiting potentials (U_L , $U_L = -\Delta G_{\text{max}}/ne$) were summarized in Fig. 5c. Generally, Cu(111) shows the lowest required potential to start multiple-electron reduction toward CO, CH_4 , and CH_3OH . However, their limiting potentials are all around -1.2 V, which results in various ECR products once the reduction process starts. Also, the low U_L (-0.20 V) for H_2 evolution is bound to cause much FE losses to competing HER on Cu(111) surface. All of these were reflected in the experimental results of CuPc. Conversely, CuN_2O_2 sites not only elevate the U_L of HER, but also differentiate the U_L of CH_4 (-2.16 V) with that of HCOOH (-1.47 V), CO (-1.56 V), and CH_3OH (-1.56 V). That makes the potential window of producing CH_4 depart from other products' to more negative bias so that CH_4 can be exclusively produced at the potential with highest FE(CH_4).

Furthermore, we also disclosed the reasons why CuN_2O_2 's copper center possesses low-valent oxidation state by calculating

its differential charge densities which depicted a less positive-charge distribution density on the Cu atom of CuN_2O_2 than that of CuN_4 (Fig. 5d, e). In addition, the calculated Bader charge uncovered that the CuN_2O_2 ($+0.87e$) carried less positive charge than CuN_4 ($+1.01e$). Because CuN_4 was previously proved to possess Cu(II) center⁴², we could infer CuN_2O_2 has Cu(I) oxidation state.

Discussion

In summary, we have developed a new partial-carbonization approach to produce a well-controlled single atomic active sites on CDs. It consists unique CuN_2O_2 sites anchored at the edge of graphitic carbons for efficient and selective ECR. The as-synthesized Cu-CD catalyst enables electrochemical CO_2 reduction to CH_4 with high Faradaic efficiency of 78%, surpassing the current MN_xC_4 SACs. The superior catalytic CH_4 selectivity at high negative bias originates from the new electronic structure of the CuN_2O_2 site, on which the HER is greatly suppressed, while the limiting step for CH_4 production requires lower energy than other reported SACs. We believe this work not only promotes a novel and general strategy to design the metal coordination environment of SACs, but also provides an essential mechanism for rationally boosting specific product selectivity.

Methods

Synthesis of Cu-CDs and pristine CDs. Cu-CDs were synthesized according to a slightly modified version of a previously reported method²⁷. In general, 1.6 g $\text{Na}_2[\text{Cu}(\text{EDTA})]\cdot 2\text{H}_2\text{O}$ was filled into a ceramic boat and placed in the center of a quartz tube, then calcined in a tube furnace at 250, 300, or 350 °C for 2 h at a heating rate of 5 °C/min under a N_2 atmosphere. After pyrolysis, 80 mL anhydrous methanol was added to extract Cu-CDs from the product. The suspension was stirring for 15 min, then centrifuged twice at a high speed (11,000g) for 20 min to remove the insoluble copper and sodium salts. The upper brown solution was filtered with 0.22 μm Titan3™ PTFE syringe filters to remove carbon fragments. Pure Cu-CD powder was obtained by drying the methanol solution at 60 °C. Pristine CDs were synthesized from $\text{Na}_2[\text{H}_2(\text{EDTA})]$ precursor using the identical pyrolysis treatment at 250 °C.

Electrochemical test. Cu-CD electrode and pristine CD electrode: To prepare Cu-CD electrode, 10 mg of Cu-CDs was dissolved in 1900 μL of methanol/water

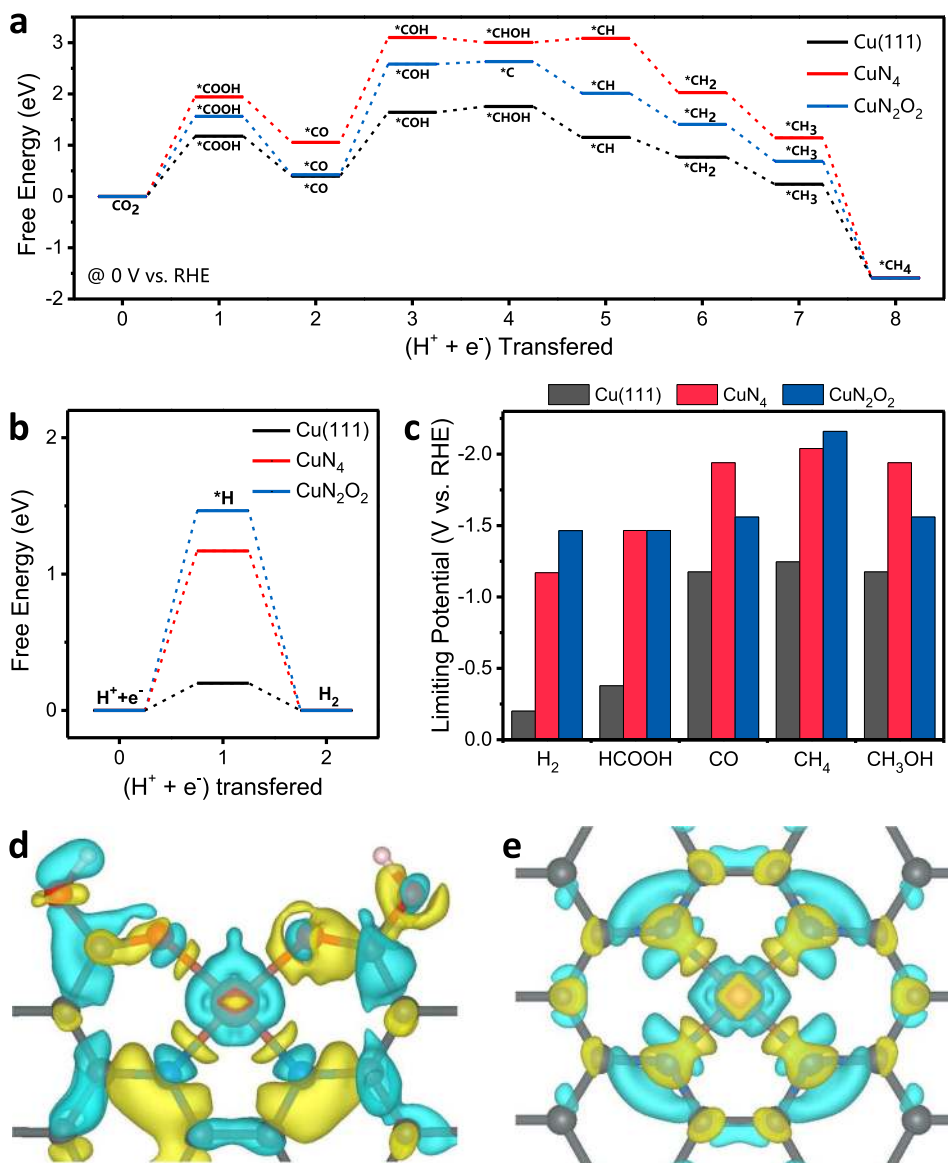


Fig. 5 Evaluation of catalytic activity by DFT simulations. Free energy diagram of the: **a** CO₂ reduction pathway to CH₄ and **b** hydrogen evolution on the CuN₂O₂(Cu-CDs), CuN₄, and Cu(111). **c** Summary of the limiting potentials of the products of ECR and HER on the CuN₂O₂, CuN₄, and Cu(111). 3D differential charge densities of: **d** CuN₂O₂ and **e** CuN₄. The yellow and blue isosurfaces correspond to the increase in the number of electrons and the depletion zone, respectively.

(1:1, v/v) mixed solvent and mixed with Nafion (100 μ L, 5 wt%) followed by vortex for 5 min; 200 μ L of catalyst ink was dropped onto the carbon paper (coated area: 7 mm \times 7 mm \times 2, loading: 1.0 mg/cm²) and dried overnight at 60 $^{\circ}$ C in a vacuum oven. CD electrode was prepared under the same procedure.

CuPc electrode: 40 mg of CuPc was mixed with 200 mL of trichloromethane by sonication for more than 30 min to form homogeneous inks. For each electrode, 200 μ L of the ink was dropped onto the carbon paper (coated area: 7 mm \times 7 mm \times 2, loading: 40 μ g/cm²) and dried overnight at 60 $^{\circ}$ C in a vacuum oven.

CDs+Cu²⁺ electrode: 10 mg of pristine CDs was dissolved in 1900 μ L of methanol/water (1:1, v/v) mixed solvent then mixed with Nafion (100 μ L, 5 wt%) and 10 μ L of CuCl₂ solution which was prepared by adding 9.3 mg of CuCl₂ in 1 mL methanol, followed by vortex for 5 min; 200 μ L of catalyst ink was dropped onto the carbon paper (coated area: 7 mm \times 7 mm \times 2, loading: 1.0 mg/cm²) and dried overnight at 60 $^{\circ}$ C in a vacuum oven.

Na₂[Cu(EDTA)] electrode: 190 μ L of the Na₂[Cu(EDTA)] solution, which was prepared by adding 30 mg Na₂[Cu(EDTA)] in 190 mL methanol/water (1:1, v/v) mixed solvent, was mixed with Nafion (10 μ L, 5 wt%) and dropped onto the carbon paper (coated area: 7 mm \times 7 mm \times 2, loading: 30 μ g/cm²) and dried overnight at 60 $^{\circ}$ C in a vacuum oven.

CO₂ reduction experiments were performed in aqueous 0.5 M KHCO₃ solution saturated with CO₂/N₂ in a twin-cell with nafion-117 membrane. All potentials were converted to those against a RHE reference:

$$E \text{ (vs. RHE)} = E \text{ (vs. Ag/AgCl)} + 0.197 \text{ V} + 0.0592 \text{ pH V}$$

Each compartment of the twin cell contained 8 mL electrolyte and approximately 10 mL headspace. The electrolytes were purged with CO₂ for 30 min (pH = 7.8) under stirring to ensure saturation before tests. With an Alicat gas controller, the flow rate of CO₂ was controlled at 15 mL/min (standard cm³/min) and routed directly into the gas sampling loop of GC. The gas phase composition was analyzed by GC every 10 min and liquid products were analyzed by ¹H NMR after test of each applied potential.

Evaluation of TOF. The TOF for CO was calculated as follows:

$$\text{TOF} = \frac{I_{\text{product}}/NF}{m_{\text{cat}} \times M_{\text{Cu}}} \times 3600 \quad (1)$$

I_{product} : partial current for certain product, CH₄;

N : the number of electron transferred for product formation, which is 8 for CH₄;

F : Faradaic constant, 96,485 C/mol;

m_{cat} : loaded catalyst mass in the electrode, g;

w : Cu loading in the catalyst, wt%;

M_{Cu} : atomic mass of Cu, 63.55 g/mol.

In situ UV-visible spectroscopy. To carry out in situ UV-visible spectroscopy, a 10 mm quartz cell was employed as an electrochemical cell. The cell was filled with electrolyte (0.5 M aqueous KHCO_3). Ag/AgCl and Pt gauze were used as reference electrode and counter-electrode, respectively. The working electrode is a 9 mm × 50 mm quartz plate with a thin Pt layer by magnetron sputtering. The catalyst ink was dropped onto the quartz plate and dried overnight at 60 °C in a vacuum oven. The schematic illustration is shown in Supplementary Fig 26. During the measurement, a series of potentials were applied to the working electrode.

Data availability

The data that support the findings of this study are available within the paper and its Supplementary Information file or are available from the corresponding authors upon request. Source data are provided with this paper.

Received: 4 July 2020; Accepted: 14 December 2020;

Published online: 26 January 2021

References

- Chen, C., Khosrowabadi Kotyk, J. F. & Sheehan, S. W. Progress toward commercial application of electrochemical carbon dioxide reduction. *Chem* **4**, 2571–2586 (2018).
- Burdyn, T. & Smith, W. A. CO_2 reduction on gas-diffusion electrodes and why catalytic performance must be assessed at commercially-relevant conditions. *Energy Environ. Sci.* **12**, 1442–1453 (2019).
- Yang, H. B. et al. Atomically dispersed Ni(i) as the active site for electrochemical CO_2 reduction. *Nat. Energy* **3**, 140–147 (2018).
- Chen, Y. et al. Single-atom catalysts: synthetic strategies and electrochemical applications. *Joule* **2**, 1242–1264 (2018).
- Wang, A., Li, J. & Zhang, T. Heterogeneous single-atom catalysis. *Nat. Rev. Chem.* **2**, 65–81 (2018).
- Zhu, W. et al. Tuning single atom-nanoparticle ratios of Ni-based catalysts for synthesis gas production from CO_2 . *Appl. Catal. B* **264**, 118502 (2020).
- Zhu, C. et al. Self-assembled Fe–N-doped carbon nanotube aerogels with single-atom catalyst feature as high-efficiency oxygen reduction electrocatalysts. *Small* **13**, 1603407 (2017).
- Pan, Y. et al. Design of single-atom Co–N5 catalytic site: a robust electrocatalyst for CO_2 reduction with nearly 100% CO selectivity and remarkable stability. *J. Am. Chem. Soc.* **140**, 4218–4221 (2018).
- Zhang, H. et al. A graphene-supported single-atom FeN5 catalytic site for efficient electrochemical CO_2 reduction. *Angew. Chem. Int. Ed. Engl.* **58**, 14871–14876 (2019).
- Wei, S. et al. Direct observation of noble metal nanoparticles transforming to thermally stable single atoms. *Nat. Nanotechnol.* **13**, 856–861 (2018).
- Fan, Q. et al. Activation of Ni particles into single Ni–N atoms for efficient electrochemical reduction of CO_2 . *Adv. Energy Mater.* **10**, 1903068 (2019).
- Fei, H. et al. General synthesis and definitive structural identification of MN4C4 single-atom catalysts with tunable electrocatalytic activities. *Nat. Catal.* **1**, 63–72 (2018).
- Hu, X.-M. et al. Selective CO_2 Reduction to CO in Water using Earth-Abundant Metal and Nitrogen-Doped Carbon Electrocatalysts. *ACS Catal.* **8**, 6255–6264 (2018).
- Gong, Y. N. et al. Regulating the coordination environment of MOF-templated single-atom nickel electrocatalysts for boosting CO_2 reduction. *Angew. Chem. Int. Ed. Engl.* **59**, 2705–2709 (2020).
- Guan, A. et al. Boosting CO_2 electroreduction to CH_4 via tuning neighboring single-copper sites. *ACS Energy Lett.* **5**, 1044–1053 (2020).
- Back, S., Lim, J., Kim, N. Y., Kim, Y. H. & Jung, Y. Single-atom catalysts for CO_2 electroreduction with significant activity and selectivity improvements. *Chem. Sci.* **8**, 1090–1096 (2017).
- Liu, J.-H., Yang, L.-M. & Ganz, E. Electrocatalytic reduction of CO_2 by two-dimensional transition metal porphyrin sheets. *J. Mater. Chem. A* **7**, 11944–11952 (2019).
- Elouarzaki, K., Kannan, V., Jose, V., Sabharwal, H.S. & Lee, J.M. Recent trends, benchmarking, and challenges of electrochemical reduction of CO_2 by molecular catalysts. *Adv. Energy Mater.* **9**, 1900090 (2019).
- Ren, S. et al. Molecular electrocatalysts can mediate fast, selective CO_2 reduction in a flow cell. *Science* **365**, 367–369 (2019).
- Wang, J. et al. A water-soluble Cu complex as molecular catalyst for electrocatalytic CO_2 reduction on graphene-based electrodes. *Adv. Energy Mater.* **9**, 1803151 (2019).
- Takeda, H., Cometto, C., Ishitani, O. & Robert, M. Electrons, photons, protons and earth-abundant metal complexes for molecular catalysis of CO_2 reduction. *ACS Catal.* **7**, 70–88 (2016).
- Jiang, J. et al. Unusual stability of a bacteriochlorin electrocatalyst under reductive conditions. a case study on CO_2 Conversion to CO. *ACS Catal.* **8**, 10131–10136 (2018).
- Savéant, J.-M. Molecular catalysis of electrochemical reactions. mechanistic aspects. *Chem. Rev.* **108**, 2348–2378 (2008).
- Wu, Y., Jiang, Z., Lu, X., Liang, Y. & Wang, H. Domino electroreduction of CO_2 to methanol on a molecular catalyst. *Nature* **575**, 639–642 (2019).
- Zhang, X. et al. Highly selective and active CO_2 reduction electrocatalysts based on cobalt phthalocyanine/carbon nanotube hybrid structures. *Nat. Commun.* **8**, 14675 (2017).
- Weng, Z. et al. Active sites of copper-complex catalytic materials for electrochemical carbon dioxide reduction. *Nat. Commun.* **9**, 415 (2018).
- Wu, W. et al. Cu–N dopants boost electron transfer and photooxidation reactions of carbon dots. *Angew. Chem. Int. Ed. Engl.* **54**, 6540–6544 (2015).
- Wu, J. et al. A metal-free electrocatalyst for carbon dioxide reduction to multi-carbon hydrocarbons and oxygenates. *Nat. Commun.* **7**, 13869 (2016).
- Baker, S. N. & Baker, G. A. Luminescent carbon nanodots: emergent nanolights. *Angew. Chem. Int. Ed. Engl.* **49**, 6726–6744 (2010).
- Guo, S. et al. Cu-CDots nanocorals as electrocatalyst for highly efficient CO_2 reduction to formate. *Nanoscale* **9**, 298–304 (2017).
- Wu, M. et al. Preparation of functionalized water-soluble photoluminescent carbon quantum dots from petroleum coke. *Carbon* **78**, 480–489 (2014).
- Wu, J. et al. Carbon dioxide hydrogenation over a metal-free carbon-based catalyst. *ACS Catal.* **7**, 4497–4503 (2017).
- Hao, G. P., Li, W. C., Qian, D. & Lu, A. H. Rapid synthesis of nitrogen-doped porous carbon monolith for CO_2 capture. *Adv. Mater.* **22**, 853–857 (2010).
- Guo, D. et al. Active sites of nitrogen-doped carbon materials for oxygen reduction reaction clarified using model catalysts. *Science* **351**, 361 (2016).
- Gayathri, P. & Senthil Kumar, A. Electrochemical behavior of the 1,10-phenanthroline ligand on a multiwalled carbon nanotube surface and its relevant electrochemistry for selective recognition of copper ion and hydrogen peroxide sensing. *Langmuir* **30**, 10513–10521 (2014).
- Huang, C. et al. Coordination mode engineering in stacked-nanosheet metal-organic frameworks to enhance catalytic reactivity and structural robustness. *Nat. Commun.* **10**, 2779 (2019).
- Stephens, F. S. Crystal and molecular structure of aquo(dihydrogen ethylenediaminetetra-acetato)copper(II). *J. Chem. Soc. A*, 1723–1734 (1969).
- Fernane, F., Mecherri, M. O., Sharrock, P., Fiallo, M. & Sipos, R. Hydroxyapatite interactions with copper complexes. *Mater. Sci. Eng. C* **30**, 1060–1064 (2010).
- Weng, Z. et al. Electrochemical CO_2 reduction to hydrocarbons on a heterogeneous molecular Cu catalyst in aqueous solution. *J. Am. Chem. Soc.* **138**, 8076–8079 (2016).
- Lee, S. Y. et al. Mixed copper states in anodized Cu electrocatalyst for stable and selective ethylene production from CO_2 reduction. *J. Am. Chem. Soc.* **140**, 8681–8689 (2018).
- Karapinar, D. et al. Electroreduction of CO_2 on single-site copper-nitrogen-doped carbon material: selective formation of ethanol and reversible restructuring of the metal sites. *Angew. Chem. Int. Ed. Engl.* **58**, 15098–15103 (2019).
- Wu, H. et al. Highly doped and exposed Cu(i)–N active sites within graphene towards efficient oxygen reduction for zinc–air batteries. *Energy Environ. Sci.* **9**, 3736–3745 (2016).

Acknowledgements

J.-J.Z. and Q.M. would like to acknowledge the International Cooperation Foundation from Ministry of Science and Technology of China (2016YFE0130100), the National Natural Science Foundation of China (21974062, 21834004), and Excellent Research Program of Nanjing University (ZYJH004). Y.L. would like to acknowledge the Washington State University Start-up Fund.

Author contributions

Y.C., Y.Z., and J.F. contributed equally to this work. Y.C. and J.F. conceived the idea and designed the experiments. Y.Z. performed the EXAFS test and analyzed the data. Y.C. and Y.Z. performed the catalytic performance evaluations. Y.C. and J.F. conducted the DFT simulation. Y.C. and Y.-C.C. collected the SEM, TEM, HRTEM, and STEM images. Y.C., Y.Z., and J.F. created figures. J.-J.Z. discussed the results and commented on the paper. Y.C., J.F., and W.Z. co-wrote the paper. Q.M., Y.L., and W.Z. supervised the whole project and involved in manuscript preparation and revision.

Competing interests

The authors declare no competing interests.

Additional information

Supplementary information is available for this paper at <https://doi.org/10.1038/s41467-020-20769-x>.

Correspondence and requests for materials should be addressed to Q.M., Y.L. or W.Z.

Peer review information *Nature Communications* thanks the anonymous reviewers for their contribution to the peer review of this work.

Reprints and permission information is available at <http://www.nature.com/reprints>

Publisher's note Springer Nature remains neutral with regard to jurisdictional claims in published maps and institutional affiliations.



Open Access This article is licensed under a Creative Commons Attribution 4.0 International License, which permits use, sharing, adaptation, distribution and reproduction in any medium or format, as long as you give appropriate credit to the original author(s) and the source, provide a link to the Creative Commons license, and indicate if changes were made. The images or other third party material in this article are included in the article's Creative Commons license, unless indicated otherwise in a credit line to the material. If material is not included in the article's Creative Commons license and your intended use is not permitted by statutory regulation or exceeds the permitted use, you will need to obtain permission directly from the copyright holder. To view a copy of this license, visit <http://creativecommons.org/licenses/by/4.0/>.

© The Author(s) 2021